PNAS RESEARCH ARTICLE | PLANT BIOLOGY

Constitutive activation of a nuclear-localized calcium channel complex in *Medicago truncatula*

Haiyue Liu[a,b,1], Jie-Shun Lin[a,b,1,2], Zhenpeng Luo[a,b,1], Jongho Sun[c,1], Xiaowei Huang[a,b,1], Yang Yang[a,b], Ji Xu[a], Yong-Fei Wang[a], Peng Zhang[a], Giles E. D. Oldroyd[c], and Fang Xie[a,3]

Edited by Maria Harrison, Cornell University, Ithaca, NY; received April 9, 2022; accepted July 14, 2022

Nuclear Ca^{2+} oscillations allow symbiosis signaling, facilitating plant recognition of beneficial microsymbionts, nitrogen-fixing rhizobia, and nutrient-capturing arbuscular mycorrhizal fungi. Two classes of channels, DMI1 and CNGC15, in a complex on the nuclear membrane, coordinate symbiotic Ca^{2+} oscillations. However, the mechanism of Ca^{2+} signature generation is unknown. Here, we demonstrate spontaneous activation of this channel complex, through gain-of-function mutations in *DMI1*, leading to spontaneous nuclear Ca^{2+} oscillations and spontaneous nodulation, in a *CNGC15*-dependent manner. The mutations destabilize a hydrogen-bond or salt-bridge network between two RCK domains, with the resultant structural changes, alongside DMI1 cation permeability, activating the channel complex. This channel complex was reconstituted in human HEK293T cell lines, with the resultant calcium influx enhanced by autoactivated DMI1 and CNGC15s. Our results demonstrate the mode of activation of this nuclear channel complex, show that DMI1 and CNGC15 are sufficient to create oscillatory Ca^{2+} signals, and provide insights into its native mode of induction.

calcium channel | CNGC15 | DMI1 | NF signaling | nuclear calcium spiking

A central feature of legumes is the root nodule symbioses with nitrogen-fixing rhizobial bacteria, which provide a direct source of fixed nitrogen. The symbiosis is initiated by rhizobial release of lipochitooligosaccharide (LCO) signaling molecules, called Nod factors (NFs), that promote a plant developmental program to accommodate rhizobia and support nitrogen fixation. Purified NFs can alone induce the formation of nodules (1). Consistently, overexpression or gain-of-function mutations in several components of the NF signal transduction pathway trigger spontaneous nodulation, including the NF receptors NFR1/5 and SYMRK (2, 3); a Ca^{2+} decoding complex, CCaMK–CYCLOPS (4–6); and the nodulation-associated transcription factor NIN (7, 8).

Symbiosis signaling allows NF recognition, but evolved from and overlaps with a more ancient symbiosis with arbuscular mycorrhizal fungi (AMF) (9). Sustained oscillations in nuclear and perinuclear Ca^{2+} are the core of symbiosis signaling, and allow receptor perception of LCOs at the root surface to activate symbiotic gene expression (10–14). The proteins responsible for symbiotic Ca^{2+} oscillations reside on the nuclear membrane: the Ca^{2+}-gated cation channels DMI1/POLLUX and CASTOR (15–17), three related cyclic nucleotide-gated channels (CNGC15s) (18), and the SERCA-type calcium ATPase (MCA8) (19). DMI1, corresponding to POLLUX and CASTOR in *Lotus japonicus* and SYM8 in *Pisum sativum*, contains four transmembrane domains and two RCK (regulator of K^+ conductance) domains (15, 16, 20). Initial studies suggested that DMI1, POLLUX, CASTOR, and SYM8 might be ion channels which may function as counterion channels to compensate for the positive charge released from the Ca^{2+} store during Ca^{2+} spiking, or to activate Ca^{2+} channels by changing the potential of nuclear membranes (15, 21, 22). However, the crystal structure of the LjCASTOR C-terminal soluble RCK domain and functional studies of channel activity revealed that LjCASTOR is a Ca^{2+}-regulated Ca^{2+} channel (17). DMI1 and the CNGC15s function in a heterocomplex, implying the complex may support synchronous activation and modulate the Ca^{2+} signal (18). While the protein complexes responsible for nuclear Ca^{2+} oscillations have been described, the mechanisms that allow these complexes to create sustained Ca^{2+} oscillations have not been resolved. *Medicago truncatula* DMI2 (also known as SYMRK in *L. japonicus*) interacts with HMGR1, a regulatory enzyme of the mevalonic acid (MVA) pathway (23). Furthermore, MVA, the product of HMGR1 activity, is sufficient to induce nuclear-associated Ca^{2+} spiking in a DMI1-dependent manner (24), suggesting that DMI1 plays an essential role in generating nuclear Ca^{2+} oscillations. Here, we identify mutations in DMI1 that spontaneously activate the channel complex leading to constitutive Ca^{2+} oscillations and resultant spontaneous nodulation. The nature of these mutations and

Significance

Ca^{2+} represents a ubiquitous and versatile secondary messenger and plays important roles in signaling pathways in eukaryotic organisms. Nuclear/perinuclear Ca^{2+} oscillations induced by Nod- or Myc- factors are key in the endosymbioses of legume plants with rhizobial bacteria and arbuscular mycorrhizal fungi. How the nuclear Ca^{2+} signal is generated is poorly understood. We have isolated a gain-of-function mutation in the ion channel DMI1 that induces spontaneous calcium oscillations and spontaneous nodules. Using structural biology and genetics, we show that breaking the interface of DMI1 RCK domains results in the channel being locked in an active form. HEK293T cells transfected with autoactivated DMI1 and CNGC15s show spontaneous channel activity. Our work provides insights into how DMI1 and CNGC15 encode nuclear Ca^{2+} oscillations.

Author contributions: H.L., Y.-F.W., P.Z., G.E.D.O., and F.X. designed research; H.L., J.-S.L., Z.L., J.S., and X.H. performed research; J.S., X.H., Y.Y., J.X., Y.-F.W., P.Z., and G.E.D.O. contributed new reagents/analytic tools; H.L., J.-S.L., Z.L., J.S., X.H., Y.Y., and F.X. analyzed data; and G.E.D.O. and F.X. wrote the paper.

The authors declare no competing interest.

This article is a PNAS Direct Submission.

[1]H.L., J.-S.L., Z.L., J.S., and X.H. contributed equally to this work.

[2]Present address: Department of Molecular Biology and Genetics, Aarhus University, DK-8000 Aarhus, Denmark.

[3]To whom correspondence may be addressed. Email: fxie@cemps.ac.cn.

This article contains supporting information online at http://www.pnas.org/lookup/suppl/doi:10.1073/pnas.2205920119/-/DCSupplemental.

Published August 16, 2022.

their function reveals the mechanism for activation of the symbiotic Ca^{2+} channel complex.

Results

DMI1 S760N Conversion Induces Spontaneous Nodulation. A spontaneous nodulation mutant, *spontaneous nodule development 1* (*spd1*), was identified by screening a mutant population generated by ethyl methanesulfonate (EMS) treatment of the nodulation-defective *M. truncatula dmi2-1* mutant. In the absence of rhizobia, wild-type (WT) and *dmi2-1* plants did not produce any nodules, while *spd1* formed elongated and white nodules (Fig. 1*A*). Microscopic analysis found that *spd1* nodules, like WT rhizobial-infected nodules, have a typical indeterminate morphology, including a persistent apical meristem and peripheral vascular bundles which are connected to the vascular system opposite xylem poles (Fig. 1 *B* and *C*) (1). Nodule number in *spd1* increased over time (Fig. 1*D*).

To identify the *spd1* mutation, *spd1* was crossed with the *M. truncatula* mapping parent A20. The F_1 plants formed white nodules in the absence of rhizobia, and the F_2 progeny segregated in an ~3:1 ratio of Nod^+ to Nod^- (384 Nod^+:84 Nod^-; $\chi^2 = 0.3887$), indicating that *spd1* is inherited as a monogenic dominant locus. Although spontaneous nodulation occurred in heterozygous plants, the phenotype is greatly reduced in homozygous mutant lines (Fig. 1 *A* and *D*). Associated with this reduction in nodulation in homozygous mutants is an overall reduction in plant growth (*SI Appendix*, Fig. S1), implying that the homozygous mutation has a negative impact on whole-plant development.

To investigate whether the *spd1* spontaneous nodulation phenotype required other NF signaling components, we crossed *spd1* with NF signal transduction pathway mutants including *nfp-1*, *dmi3-1*, *ern1-1*, and *nin-1*; double mutants were identified, and the spontaneous nodulation phenotypes were analyzed. The results revealed that spontaneous nodulation was independent of the NF receptor components *NFP* and *DMI2* but dependent on the calcium decoder *CCaMK* (*DMI3*) and symbiotic transcription factors *ERN1* and *NIN* (*SI Appendix*, Fig. S2), placing SPD1 between NF recognition and the

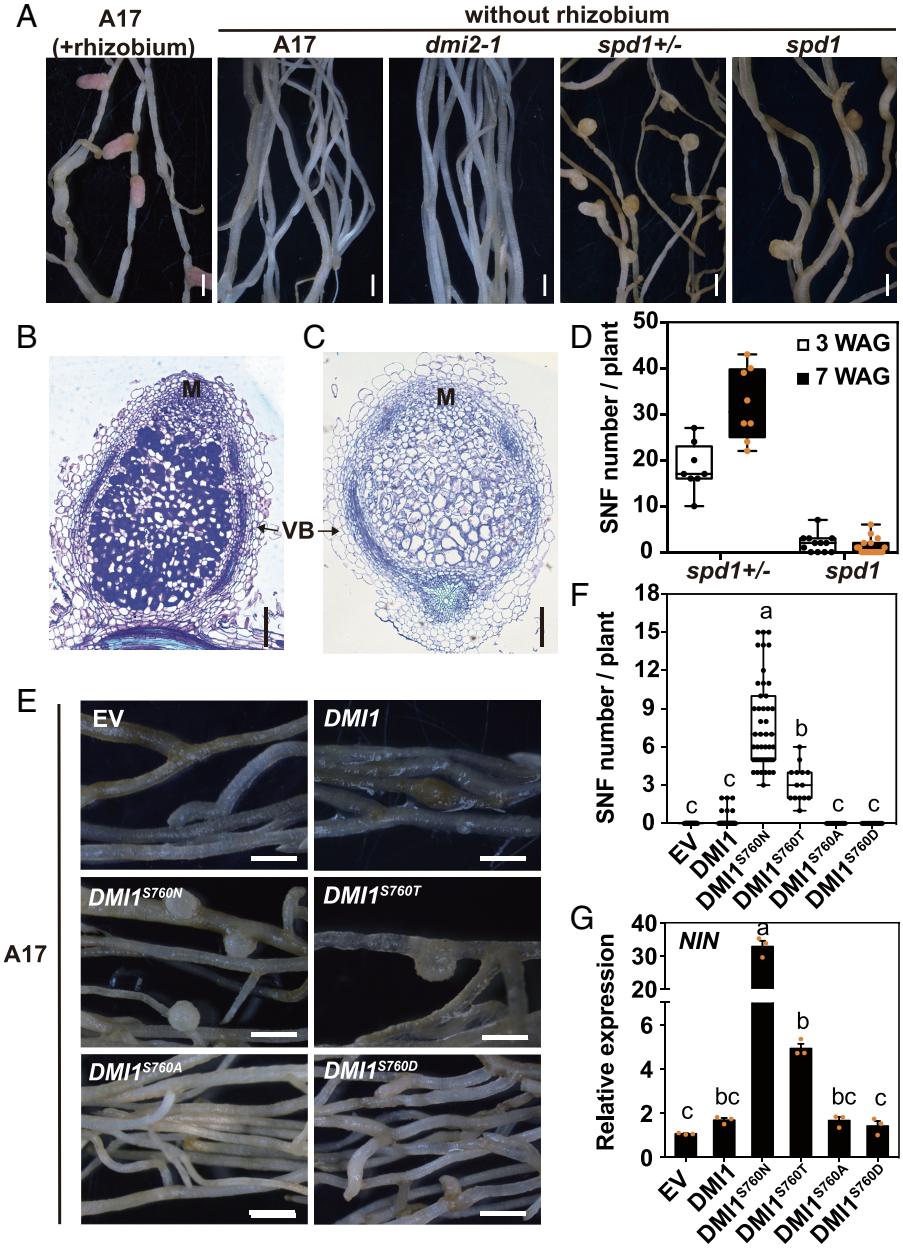

Fig. 1. *DMI1*^{S760N} confers spontaneous nodulation in *M. truncatula*. (*A*) Nodule phenotypes of *M. truncatula* WT (A17) inoculated with rhizobia, and A17, *dmi2-1*, and *spd1* heterozygotes (*spd1*$^{+/-}$) and homozygotes (*spd1*) grown under low-nitrogen conditions in the absence of rhizobia. (Scale bars, 1 mm.) (*B* and *C*) Transverse sections of a rhizobia-induced root nodule on WT (*B*) and a spontaneous root nodule on an *spd1* heterozygote (*C*). Peripheral vascular bundles (VB) are indicated by arrows. M, nodule meristem. (Scale bars, 100 μm.) (*D*) Spontaneous nodule formation (SNF) on roots of *spd1* mutants 3 or 7 wk after germination (WAG). (*E* and *F*) Spontaneous nodules (*E*) and their quantification (*F*) in composite plants expressing either *DMI1* or a series of *DMI Ser760* mutants. EV, empty vector. (Scale bars, 1 mm.) (*G*) qRT-PCR of *NIN* in transgenic roots from *E*. Letters denote significance groupings ($P < 0.05$, one-way ANOVA test). Error bars represent SE (n = 3).

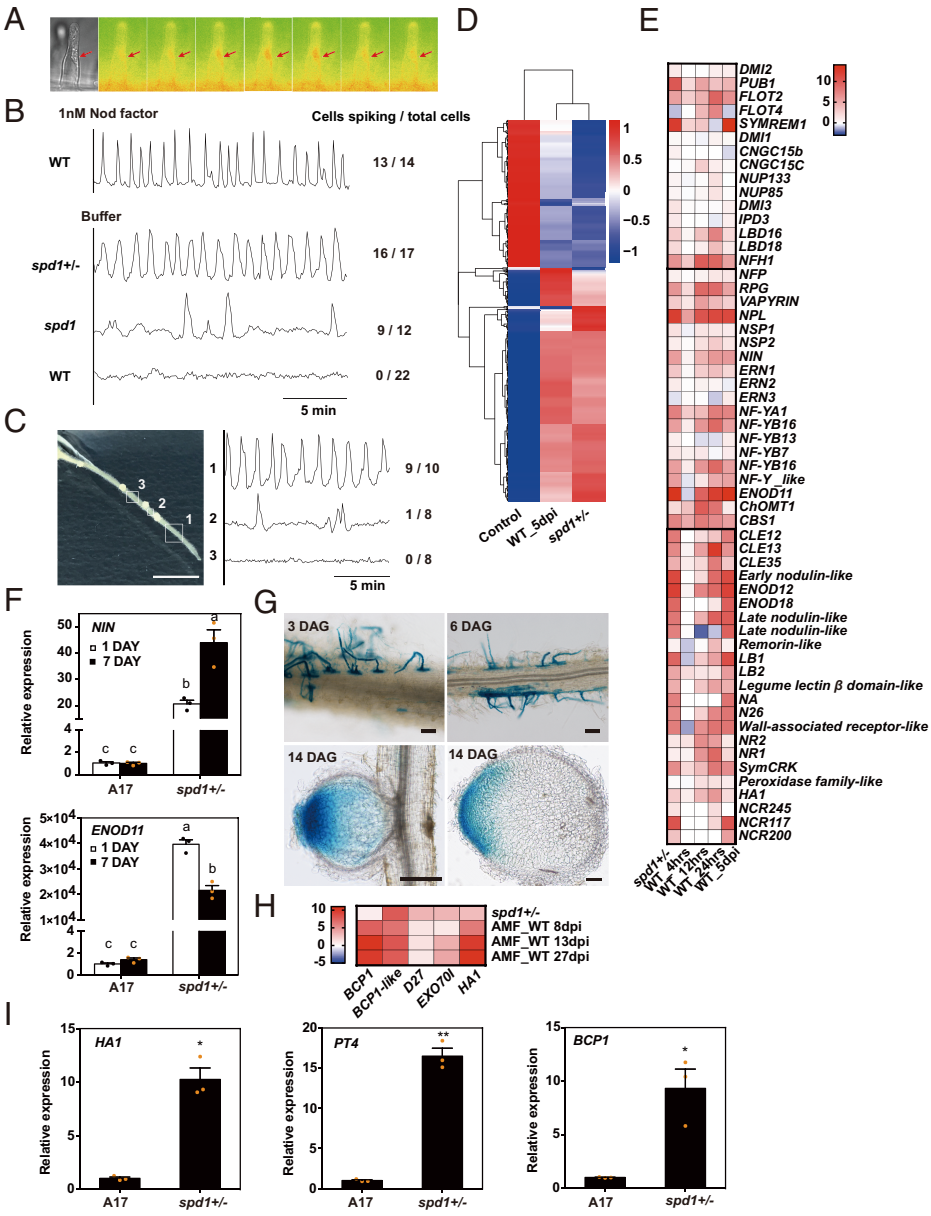

Fig. 2. *DMI1*^{S760N} constitutively activates symbiotic signaling. (*A*) Representative images of Ca^{2+} oscillations observed in the nuclear regions of *spd1*$^{+/-}$ root hairs in the absence of rhizobia or NF. Arrows indicate the nucleus. Images were taken every 5 s over a single Ca^{2+} transient. (*B* and *C*) Representative Ca^{2+} traces of NF-treated WT root hairs and untreated root hairs of *spd1*$^{+/-}$ and *spd1* seedlings (*B*), and from root hairs of the indicated regions on *spd1*$^{+/-}$ roots in the absence of NF (*C*). The *y* axis represents the yellow fluorescent protein (YFP)/CFP ratio. Numbers denote responsive cells relative to total cells analyzed. (*D*) Clustering of genes induced by rhizobia at 5 dpi in WT and constitutively expressed in *spd1*$^{+/-}$ at 7 d post germination. Genes expressed in WT at 7 d post germination were used as the control [$|\log_2(FC)| \geq 1$, $P \leq 0.05$]. FC, fold change. (*E* and *H*) Heatmaps showing selected rhizobia/NF– (*E*) and AMF-induced (*H*) genes which were constitutively expressed in *spd1*$^{+/-}$ (without rhizobia) and WT treated with rhizobia/NF (*E*) or AMF (*H*) at different time points. Expression depicts $\log_2$ FCs [$|\log_2(FC)| \geq 1$, $P \leq 0.05$]. The colored bars represent the expression values. (*F* and *I*) qRT-PCR analysis of representative symbiotic genes in *spd1*$^{+/-}$ roots in the absence of rhizobia (*F*) or AMF (*I*). WT and *spd1*$^{+/-}$ seedlings were grown on BNM and harvested at 1 or 7 d post germination (*F*) or 3 wk post germination (*I*). Letters denote significance groupings ($P < 0.05$, one-way ANOVA test). Asterisks indicate statistical differences (*$P < 0.05$, **$P < 0.01$, Student *t* test). Error bars represent SE (n = 3). (*G*) Roots of *spd1*$^{+/-}$ transformed with *ENOD11*p:GUS showing GUS activity in the absence of rhizobia. DAG, days after germination. (Scale bars, 100 μm.)

nuclear Ca^{2+} decoding, implying it is associated with the nuclear channel complex.

Genetic mapping and in silico map by sequencing revealed that the mutation in *SPD1* is located between h2_24f21b and MtB84 on chromosome 2 (*SI Appendix*, Fig. S3*A*), in a region containing *DMI1*. Sequencing of *DMI1* in *spd1* revealed a missense mutation, G4854A, which results in the substitution S760N in the C-terminal RCK2 domain (*SI Appendix*, Fig. S3 *B* and *C*). Constitutive expression of *DMI1*^{S760N} in *M. truncatula* hairy roots resulted in spontaneous nodulation, validating the cause of the *spd1* phenotype (Fig. 1 *E* and *F* and *SI Appendix*, Fig. S3 *D* and *E*).

***DMI1*^{S760N} Constitutively Activates Symbiotic Signaling.** Nuclear Ca^{2+} oscillations are a feature of the common symbiotic signaling pathway, and DMI1 is part of the nuclear-associated Ca^{2+} channel complex (10, 25). Using the nuclear-localized Ca^{2+} sensor yellow cameleon version 3.6 (YC3.6) (25) in *spd1*, we observed spontaneous nuclear Ca^{2+} oscillations (Fig. 2 *A* and *B*), preferentially in heterozygous lines (*spd1*$^{+/-}$) (Fig. 2*B*). This response was restricted to root epidermal cells in the so-called infection zone where root nodules are known to initiate, and no Ca^{2+} oscillations were found in regions that contained developed nodules or in any other region of the plant (Fig. 2*C* and *SI Appendix*, Table S1). Like NF-inducible Ca^{2+} oscillations (26, 27), the spontaneous oscillations in *spd1* were blocked by the inhibitor cyclopiazonic acid that targets SERCA-type Ca^{2+} ATPases (*SI Appendix*, Fig. S4*A*) (26). Our results demonstrate that *spd1* constitutively activates nuclear Ca^{2+} oscillations in the root region where nodules normally form.

Comparing the transcriptomes of uninoculated heterozygous roots of WT plants 5 d post inoculation (dpi) with *Sinorhizobium meliloti* 1021 revealed a high overlap (>50%) between the differentially expressed genes (DEGs) by rhizobia inoculation in WT and *spd1* roots without rhizobia inoculation (Fig. 2*D* and *SI Appendix*, Fig. S4*B*). Comparing our RNA-sequencing (RNA-seq) profiles with previous studies of NF-regulated genes (28) revealed a number of genes with known roles in NF signaling, rhizobial infection, nodule organogenesis, autoregulation of nodulation (AON), and nitrogen fixation that were induced by *spd1* (Fig. 2*E* and *SI Appendix*,

Fig. S4*B*). qPCR analysis validated that *NIN* and *ENOD11* were constitutively expressed in the *spd1* roots, even at 1 d after germination (Fig. 2*F*). Analysis of *spd1* lines carrying the symbiotic reporter *ENOD11*p:GUS showed expression specifically in root hairs and the meristem zone of elongated nodules (Fig. 2*G*), similar to *ENOD11* expression patterns observed after inoculation with rhizobia (29).

DMI1 is required for symbiotic interactions with both rhizobia and AMF (16) and our RNA-seq data showed that a series of AMF-induced genes were also activated (Fig. 2*H*). qPCR results confirmed that the AMF-induced genes *HA1*, *BCP1*, and *PT4* were constitutively expressed in $spd1^{+/-}$ (Fig. 2*I*). A comparison with published RNA-seq data (30) revealed further overlap between $spd1^{+/-}$ and AMF-specific genes (*SI Appendix*, Fig. S4*C*). However, the overlap between $spd1^{+/-}$ and AMF-induced genes was less than with NF-induced genes, possibly because of the different time points analyzed for these two interactions. This indicates that $DMI1^{S760N}$ constitutively activates rhizobial- and mycorrhizal-associated gene expression through activation of symbiotic Ca^{2+} oscillations and promotion of symbiosis signaling.

Disruption of the DMI1 Assembly Interface between RCK1 and RCK2 Domains Can Produce Spontaneous Nodules. The serine mutation in $DMI1^{S760N}$ suggested loss of phosphorylation may explain the effect; however, phospho-dead or phospho-mimetic substitutions of S760 did not induce spontaneous nodulation, while S760T activated spontaneous nodulation and *NIN* expression but at a lower efficiency (Fig. 1 *E–G* and *SI Appendix*, Fig. S3 *D* and *E*). These results show no evidence for phosphorylation at Ser760, explaining the gain-of-function effect of mutating this residue.

To understand the effect of the $DMI1^{S760N}$ mutation, we determined the structure of the soluble C terminus of DMI1. The overall structure was found to be very similar to its *L. japonicus* homolog CASTOR, with tandem RCK1 and RCK2 domains that form a subunit and four subunits that assemble into a complex that forms a tetrameric gating ring (17) (Fig. 3 *A* and *B*). Ser760 is located at the interface between the RCK1 and RCK2 domains (Fig. 3 *B* and *C1*), where several salt bridges or hydrogen bonds are predicted to stabilize the structure: two salt bridges between K420 and E458 and between R718 and D778, and two hydrogen bonds between R718 and D778 and between R448 and S708 (Fig. 3 *B* and *C2–C4*). These residues are conserved in DMI1 across many species (*SI Appendix*, Fig. S5). We hypothesized that S760N replacement affected the interaction between $RCK1_A$ and $RCK2_B$ (Fig. 3*B*), possibly locking DMI1 in an active form. Consistently, D418A, K420A, D778A, R448A, and T767K mutations all resulted in spontaneous nodulation and induction of *NIN* and *ENOD11* expression (Fig. 3 *D* and *E* and *SI Appendix*, Fig. S6). This demonstrates a network of residues that stabilize an inactivated form of DMI1, with activation resulting from a breach of this stabilized structure, with resultant activation of Ca^{2+} oscillations and spontaneous nodulation.

***$DMI1^{S760N}$* Activation of Spontaneous Nodulation Requires the DMI1 Ca^{2+}-Binding Gating Ring.** The Ca^{2+}-binding gating ring in LjCASTOR RCK domains is essential for nodule development and Ca^{2+} spiking (17). We investigated whether the Ca^{2+}-binding gating ring is essential for the spontaneous nodulation of *spd1* by mutating the Ca^{2+}-binding gating ring D470A, E521A, or E521Q in $DMI1^{S760N}$ and expressing these variants in WT roots. The results showed that $DMI1^{S760N\ D470A}$, $DMI1^{S760N\ E521A}$, and $DMI1^{S760N\ E521Q}$ did not induce spontaneous nodules or induction of *NIN* and *ENOD11* (Fig. 3 *F* and *G* and *SI Appendix*, Fig. S7), suggesting that the Ca^{2+} binding of *DMI1* is essential for $DMI1^{S760}$-mediated gain-of-function activity.

$DMI1^{S760N}$ Can Activate CNGC15 Channel Activity in HEK293T Cells. DMI1 is proposed to function in a complex with CNGC15s at the nuclear membrane (18). $DMI1^{S760N}$ still localizes to the nuclear membrane (*SI Appendix*, Fig. S8 *A* and *B*) and interacts with CNGC15b (*SI Appendix*, Fig. S8 *C–F*). However, $DMI1^{S760N}$ showed significantly fewer and smaller spontaneous nodules and less gene induction in *cngc15b* and *cngc15c* mutants or following *CNGC15b* RNA interference (RNAi) (Fig. 4 *A–D* and *SI Appendix*, Fig. S9 *A–D*). These results are equivalent to the reduction in nodules observed in these mutants when inoculated with rhizobia (18). Moreover, knockdown of *CNGC15s* expression in $spd1^{+/-}$ YC3.6 using *CNGC15b* RNAi almost completely abolished spontaneous Ca^{2+} oscillations, with only a few rare cells showing very poor oscillations (3/37) (Fig. 4*E* and *SI Appendix*, Fig. S9*E*). We infer that the rare remaining activity in these RNAi lines results from incomplete suppression of *CNGC15s*, as oppose to alternative mechanisms of DMI1 action, although this cannot be excluded. We conclude that $DMI1^{S760N}$ is dependent on CNGC15s to activate nodulation, consistent with DMI1 and CNGC15s acting in a complex to coordinate symbiotic Ca^{2+} oscillations.

To determine the interplay between DMI1 and CNGC15s in generating Ca^{2+} signals, we investigated its cytosolic Ca^{2+} channel activity using HEK293T cells by monitoring the ratio (535 nm/480 nm) of the calcium indicator YC3.6 upon application of 10 mM external $CaCl_2$. It was reported previously that DMI1-GFP (green fluorescent protein) localizes to the nuclear envelope of HEK293 cells, and that the transformed cells displayed perinuclear Ca^{2+} oscillations following exogenous Ca^{2+} treatment (22). We found that expression of DMI1 or CNGC15b alone in HEK293T cells resulted in small increases in cytosolic Ca^{2+}, with $DMI1^{S760N}$ or $DMI1^{R448A}$ showing incremental increases, and that this increase was abolished in $DMI1^{S760N\ E521A}$, in which DMI1 gating ring Ca^{2+} binding was lost (Fig. 5*A* and *SI Appendix*, Figs. S10*A* and S11 *A–E*). Coexpression of DMI1 and CNGC15b resulted in similar cytosolic Ca^{2+} levels as CNGC15b alone (Fig. 5*B* and *SI Appendix*, Figs. S10*B* and S12 *A* and *B*). However, the combination of $DMI1^{S760N}$ or $DMI1^{R448A}$ and CNGC15b resulted in dramatic increases in cytosolic Ca^{2+} levels, and half of the experiments exhibited distinct oscillatory behavior (Fig. 5 *B* and *C* and *SI Appendix*, Figs. S10*B* and S12 *D–E′*). Such oscillations did not occur in any other combination where cytosolic Ca^{2+} release was observed. Moreover, this increase in cytosolic Ca^{2+} was abolished in $DMI1^{S760N\ E521A}$, in which the DMI1 gating ring lacked Ca^{2+}-binding activity, when coexpressed with CNGC15b in HEK293T cells (Fig. 5*D* and *SI Appendix*, Figs. S10*B* and S12*F*). The external application of 200 μM gadolinium (Gd^{3+}), a well-known blocker of Ca^{2+} channels, completely abolished cytosolic Ca^{2+} accumulation (*SI Appendix*, Fig. S10*C*). A similar increase in cytosolic Ca^{2+} accumulation was detected when $DMI1^{S760N}$ or $DMI1^{S760N\ E521A}$ variants were coexpressed with CNGC15c in HEK293T cells (*SI Appendix*, Figs. S10*D*, S11*H*, and S12 *C*, *G*, and *H*).

LjCASTOR D265 plays an important role in Ca^{2+} selectivity, and a D265N mutation completely abolishes its channel activity (17). MtDMI1 D293 corresponds to LjCASTOR D265 (*SI Appendix*, Fig. S5), and expression of $DMI1^{S760N\ D293N}$ in

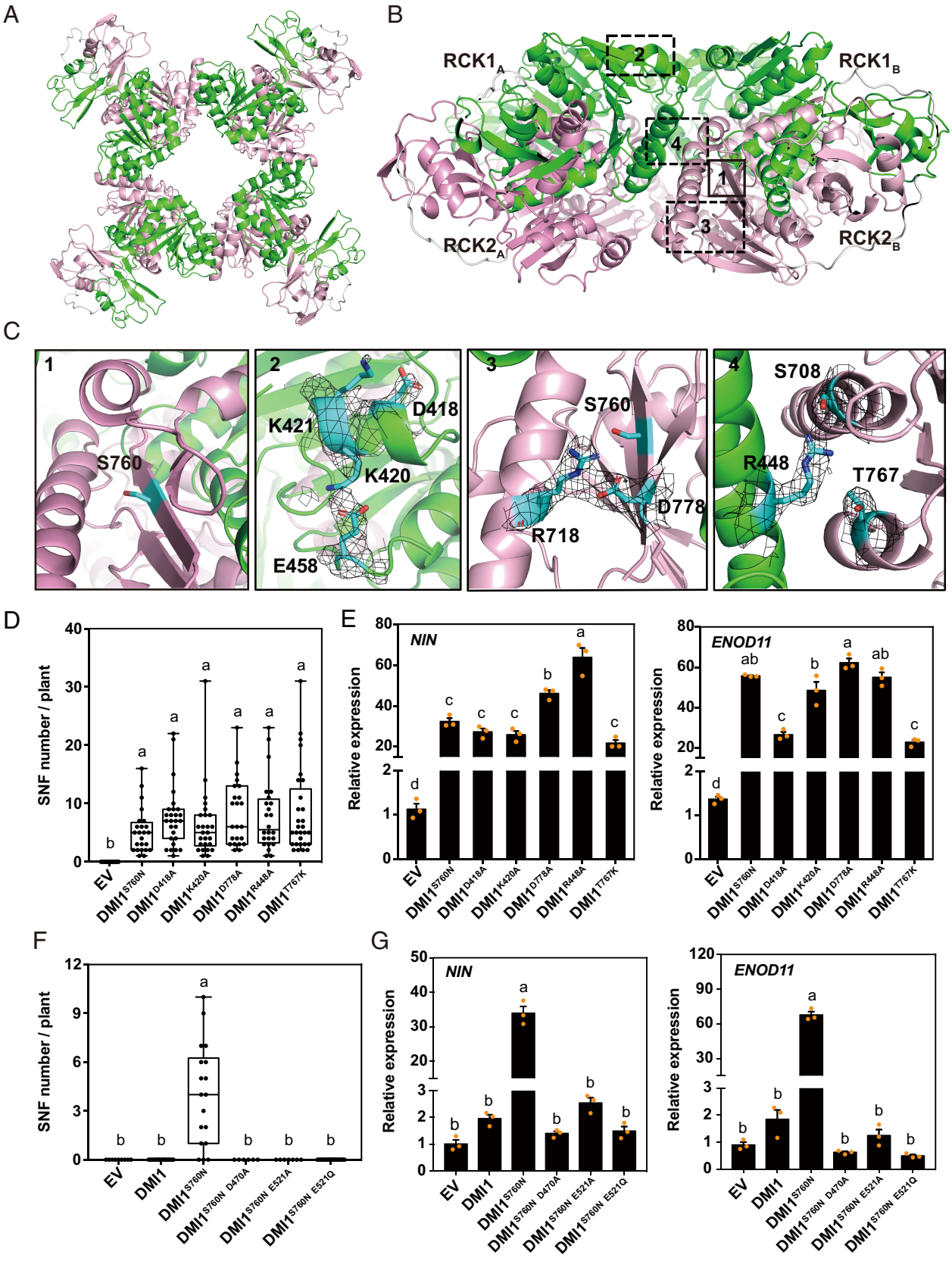

Fig. 3. Mutations in the DMI1 assembly interface trigger spontaneous nodule formation. (*A*) Top view of the crystal structure of the DMI1 C-terminal soluble subunit showing the gating ring. (*B*) Side view showing the RCK1–RCK2 domain interface. Colors show RCK domains. (*C*) Higher-resolution views of the boxed regions in *B*: residues in the assembly interface involved in formation of hydrogen bonds or salt bridges. The electron density (gray mesh contoured at 1 σ) of residues is calculated from the 2Fo − Fc map. (*D* and *F*) Spontaneous nodules formed on transgenic roots expressing *DMI1* with mutations predicted to disrupt the assembly interface network (*D*) or on roots expressing *DMI1*^{S760N} containing Ca^{2+}-binding site mutations (*F*). (*E* and *G*) qRT-PCR analysis of *NIN* and *ENOD11* expression in transgenic roots of *D* and *F*. Letters denote statistical groups ($P < 0.05$, one-way ANOVA test). Error bars represent SE (n = 3).

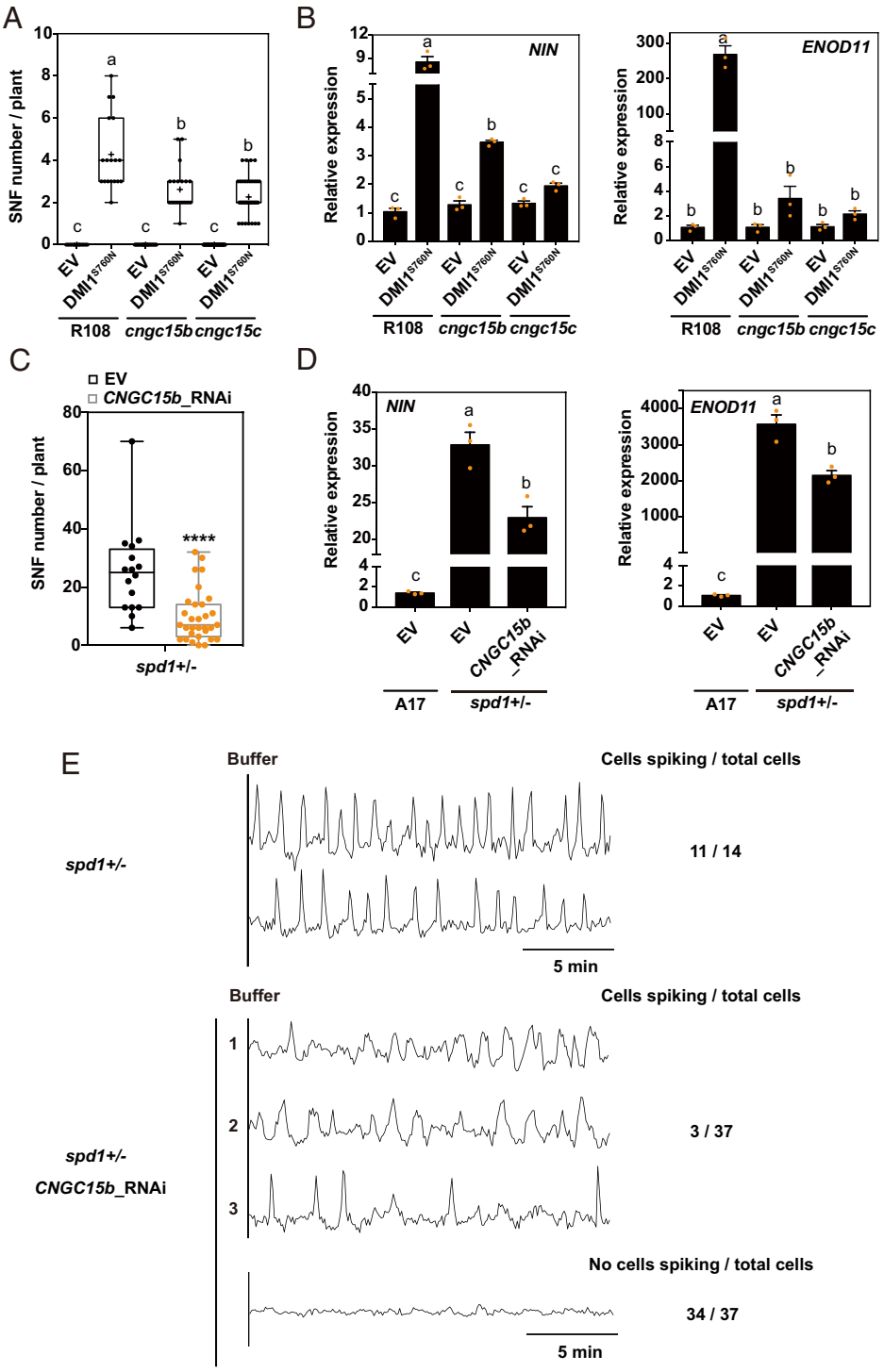

Fig. 4. CNGC15s are required for *DMI1*^{S760N}-activated spontaneous nodulation and Ca^{2+} spiking. (*A*–*D*) Spontaneous nodule numbers (*A* and *C*) and *NIN* and *ENOD11* expression (*B* and *D*) on transgenic roots expressing *DMI1*^{S760N} in R108 (WT), *cngc15b-1* and *cngc15c-1* (*A* and *B*), or *CNGC15b* RNAi in *spd1*$^{+/-}$ (*C* and *D*) in the absence of rhizobia. Letters indicate statistical groups ($P < 0.05$, one-way ANOVA test). Asterisks indicate statistical differences (****$P < 0.0001$, Student *t* test). Error bars represent SE (n = 3). (*E*) Representative Ca^{2+} traces of *CNGC15b* RNAi in *spd1*$^{+/-}$ transgenic roots in the absence of NF. The *y* axis represents the YFP/CFP ratio. Numbers denote responsive cells relative to total cells analyzed.

M. truncatula hairy roots did not form spontaneous nodules (*SI Appendix*, Fig. S10 *E* and *F*). Coexpression of DMI1^{S760N} ^{D293N} and CNGC15b/c showed no increase in cytosolic Ca^{2+} levels in HEK293T cells (Fig. 5*E* and *SI Appendix*, Figs. S10*B* and S12 *I* and *J*), suggesting that DMI1 channel activity was essential for the DMI1^{S760N}/CNGC15b/c–induced Ca^{2+} release. CNGC15s are predicted Ca^{2+}-permeable channels (18), and coexpression of DMI1^{S760N} with two loss-of-function mutations of CNGC15b (CNGC15b^{R504Q} and CNGC15b^{G346E}) (31, 32) did not show Ca^{2+} release in HEK293T cells (Fig. 5*E* and *SI Appendix*, Figs. S10*B* and S12 *K* and *L*). Consistently, these loss-of-function mutations of *CNGC15b* cannot rescue *cngc15b* nodulation deficiencies after rhizobia inoculation (*SI Appendix*, Fig. S13). We conclude the channel activities of both DMI1 and CNGC15s are essential to facilitate Ca^{2+} release from this channel complex.

***DMI1*^{S760N} Does Not Respond to NF and Rhizobia Inoculation.** *L. japonicus snf1* and *snf2* can form mature pink nodules after rhizobia inoculation (4, 33). However, neither heterozygous nor homozygous *spd1* plants could be infected by rhizobia and were thus unable to form infected nodules (Fig. 6*A*). In addition, NF- and rhizobia-induced root hair deformation did not occur in *spd1*$^{+/-}$ (Fig. 6 *B* and *C*). Consistent with this, *spd1* nodule number did not change after rhizobia inoculation (*SI Appendix*, Fig. S14 *A* and *B*).

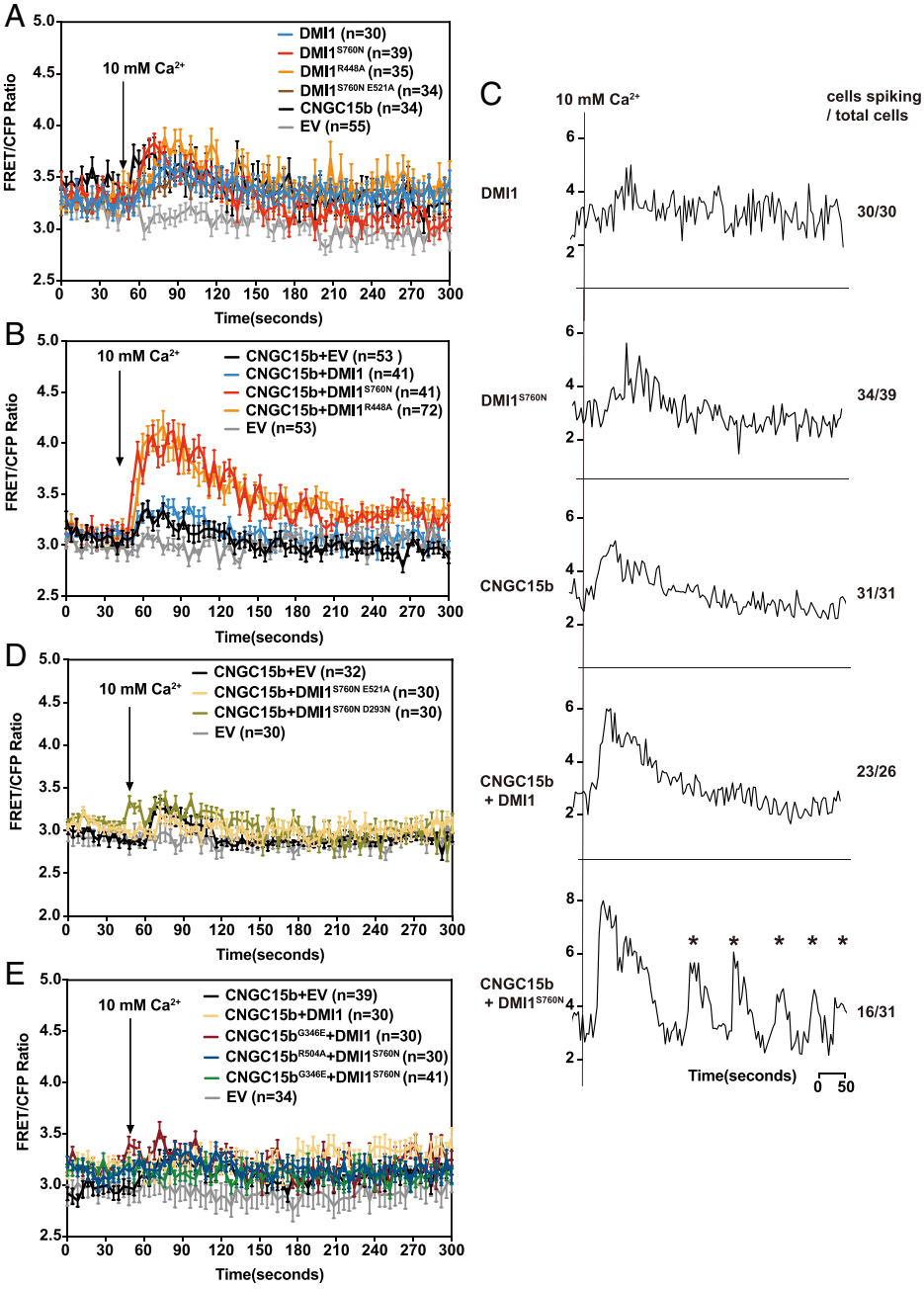

Fig. 5. Coexpression of gain-of-function DMI1 and CNGC15b in HEK293T cells enhances cytosolic Ca^{2+} levels. (*A*, *B*, *D*, and *E*) Average YC3.6 fluorescence ratios (535 nm/480 nm) of HEK293T cells transiently expressing the indicated proteins over time. YC3.6 (EV) was used as a control. The experiments were repeated at least three times, and *n* represents the number of cells examined. Error bars represent SE (n ≥ 30). (*C*) Representative Ca^{2+} traces of expression of DMI1, $DMI1^{S760N}$, or CNGC15b alone or coexpression in HEK293T cells. The *y* axis represents the YFP/CFP ratio. Numbers denote responsive cells relative to total cells analyzed. The asterisks indicate Ca^{2+} traces which have oscillation.

Overexpression of *DMI1* can induce some small nodule-like bumps, an effect that increased over time (Fig. 6*D* and *SI Appendix*, Fig. S14 *C–E*). The symbiotic genes *NIN* and *ENOD11* were also induced in *DMI1* overexpression roots, but the gene induction level was lower than $DMI1^{S760N}$, as was the number of nodule-like bumps that formed (Fig. 6 *E* and *F*). However, overexpression of *CNGC15b* did not induce the formation of nodule-like bumps or symbiotic gene expression (*SI Appendix*, Fig. S14 *F–H*). These results demonstrate that the overexpression of *DMI1*, but not *CNGC15b*, results in the partial activation of the symbiotic pathway, similar to what has been reported for symbiotic receptor-like kinases (2).

Discussion

Nuclear Ca^{2+} oscillations sit at the core of symbiotic signaling and are the result of a channel complex residing on the nuclear envelope (10, 12, 18). Here, we demonstrate that *spd1*, a gain-of-function mutation in *DMI1*, can constitutively activate symbiosis signaling leading to nodule formation in the absence of rhizobia. We show that $DMI1^{S760N}$ locks this channel in its active form, constitutively promoting CNGC15 channel activity and thereby Ca^{2+} oscillations.

During plant–microbe symbiotic interactions, NF or Myc factor signaling can activate nuclear Ca^{2+} oscillations. However, while the NF or Myc factor receptors are localized in the plasma membrane, the ion channels DMI1 and CNGC15 are localized in the nuclear membrane. MVA or some of its downstream products were suggested as a possible second messenger since it can induce Ca^{2+} spiking in DMI1-expressing HEK293T cells (24). CASTOR, a DMI1 homolog in *L. japonicus*, was shown to function as a Ca^{2+}-regulated Ca^{2+} channel (17), but the role of DMI1 in encoding the nuclear Ca^{2+} signals was unproven. In *Arabidopsis thaliana*, AtCNGC2 and AtCNGC4 interact and assemble into a functional Ca^{2+} channel (31); AtCNGC7/8 and AtCNGC18 are active as heteromeric channels (34), and SLAC1

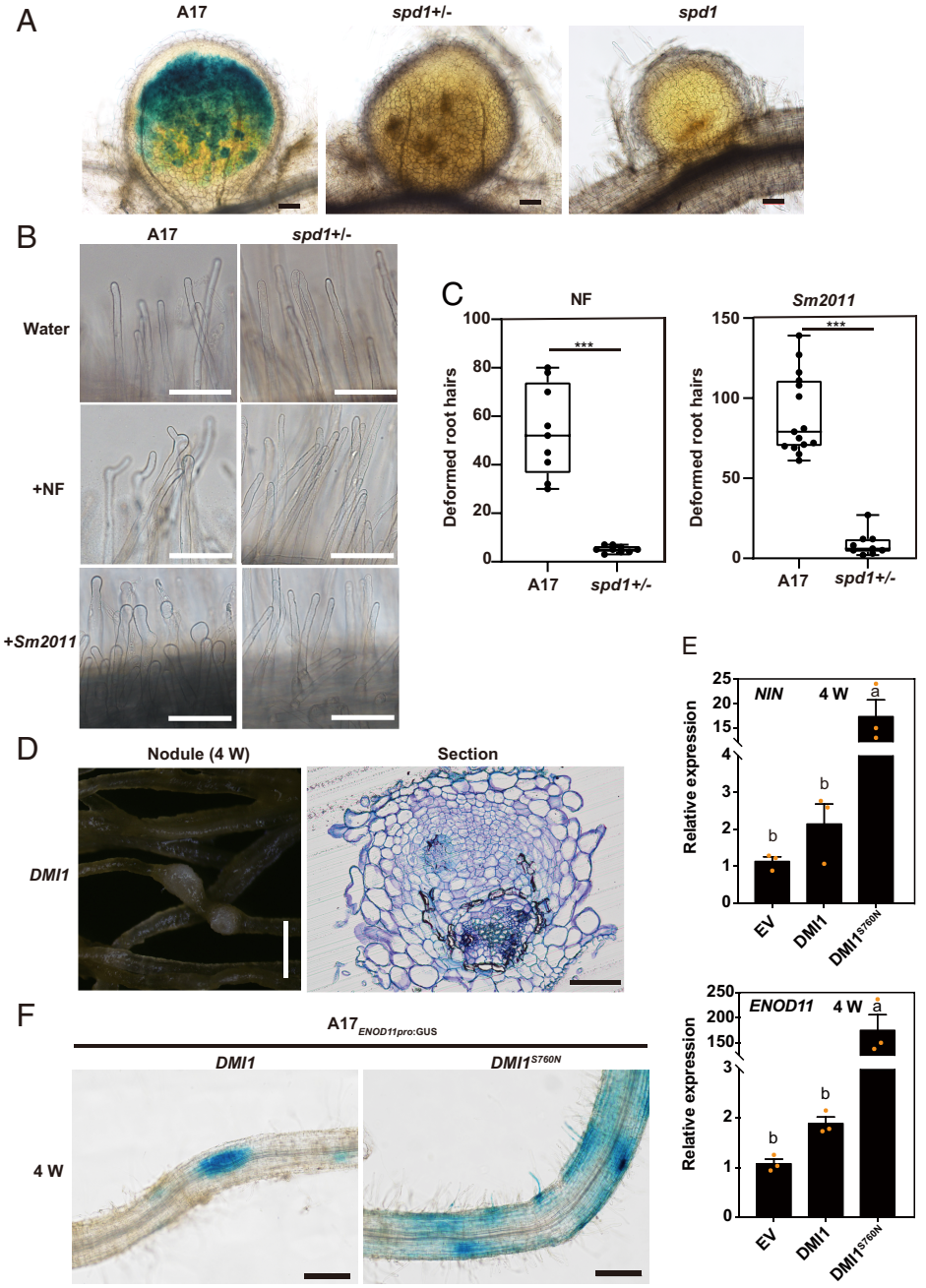

Fig. 6. *spd1* is insensitive to NF or rhizobia inoculation, and overexpression of *DMI1* can form spontaneous bumps. (*A*) Nodule phenotype of WT (A17), *spd1*$^{+/-}$, and *spd1* 7 d after being inoculated with *Sm2011* (carrying pXLGD4). Histochemical analysis of root staining using X-gal. (*B* and *C*) Root hair deformation images (*B*) and numbers (*C*) in A17 and *spd1*$^{+/-}$ after NF or rhizobia inoculation (24 or 36 h). (Scale bars, 100 μm.) Asterisks indicate statistical differences (**P < 0.01, ***P < 0.001, Student t test). (*D*–*F*) Spontaneous nodule phenotype (*D*) and symbiotic gene expression (*E* and *F*) in *DMI1* overexpression roots. Letters denote statistical groups (P < 0.05, one-way ANOVA test). (Scale bars, 1 mm.) Error bars represent SE (n = 3).

interacts with SLAC3 to inhibit the inward-rectifying K^+ channel KAT1 and prevent stomatal opening (35). CNGC15 Ca^{2+} channels associate with DMI1 at the nuclear envelope where they mediate Ca^{2+} spiking (18), suggesting the function of these two channels is coordinated. In contrast to previous studies, in our system, expression of DMI1 alone was not sufficient to induce Ca^{2+} oscillations in HEK293 cells (17, 22). This difference might result from differences between the constructs or treatments used. However, our study found that coexpression of the dominant DMI1 (DMI1^{S760N} or DMI1^{R448A}) with CNGC15b/c in HEK293T cells greatly increased Ca^{2+} accumulation, and this increase was dependent on the activity of the DMI1 Ca^{2+}-binding gating ring and the channel activity of both DMI1 and CNGC15b. Our work highlights the importance of both DMI1 and CNGC15s for promoting calcium responses in HEK293 cells. While these two channels have been shown to interact in vitro and in vivo (18), there is currently no proof that they interact in HEK293 cells.

In contrast with other spontaneous nodulation mutants (4, 33), *spd1* was insensitive to NF treatment and does not show rhizobial infection. This defect may result from inhibition of the common symbiotic signaling pathway resulting from overactivation of the AON pathway, such has been reported for overexpression of *NIN* (36). Interestingly, an analogous phenomenon was reported for the *L. japonicus SNF2* gain-of-function cytokinin receptor mutant, which displayed a cytokinin-activated phenotype but was unable to respond to cytokinin (33). Nuclear Ca^{2+} oscillations only occurred in *spd1* at nodule initiation sites, which is consistent with the expression of *ENOD11* in both *spd1* and upon NF or rhizobial treatment (29). Considering that *spd1* is autoactivated for symbiosis signaling and is expressed from its native promoter, we conclude that the promotion of symbiosis signaling must be restricted to a small number of epidermal cells near the tip of growing roots. The similarities we see between the patterns of *ENDO11* expression and calcium induction in *spd1* lead us to

propose that the cellular restriction of symbiosis signaling in *spd1* is indicative of the activation of this pathway in its normal context. Heterozygous *spd1* plants were healthier than homozygous mutants, showed regular Ca^{2+} oscillations, and also produced more nodules. This suggests that homozygous *spd1* is very detrimental to plant development, perhaps because of abnormally high levels of Ca^{2+} in the cytoplasm/nucleoplasm which may cause toxicity. This resembles the developmental effect of a gain-of-function *CNGC* mutation (*brush*) in *L. japonicus* which resulted in a leaky tetrameric channel (37, 38).

We propose that, upon rhizobial or mycorrhizal recognition at the root surface by the plasma membrane–associated receptor complex, a secondary messenger is released that directly or indirectly activates conformational changes in DMI1 at the nuclear envelope, which promotes the channel activity of CNGC15s to trigger nuclear Ca^{2+} oscillations (Fig. 7*A*). $DMI1^{S760N}$ or other gain-of-function DMI1 variants disrupt the interface assembly, which constitutively opens the channel and mimics the normal activation of DMI1 during symbiosis signaling (Fig. 7*B*). Ca^{2+} oscillations in $DMI1^{S760N}$ are restricted to root epidermal cells at nodule initiation sites, highlighting the restricted nature of symbiosis signaling to a specific cell type within a restricted region of the root. Activation of the symbiotic channel complex in epidermal cells is still sufficient to promote nodule organogenesis in the cortex, highlighting the coordinated nature of nodule development at a distance from the site of symbiosis signaling.

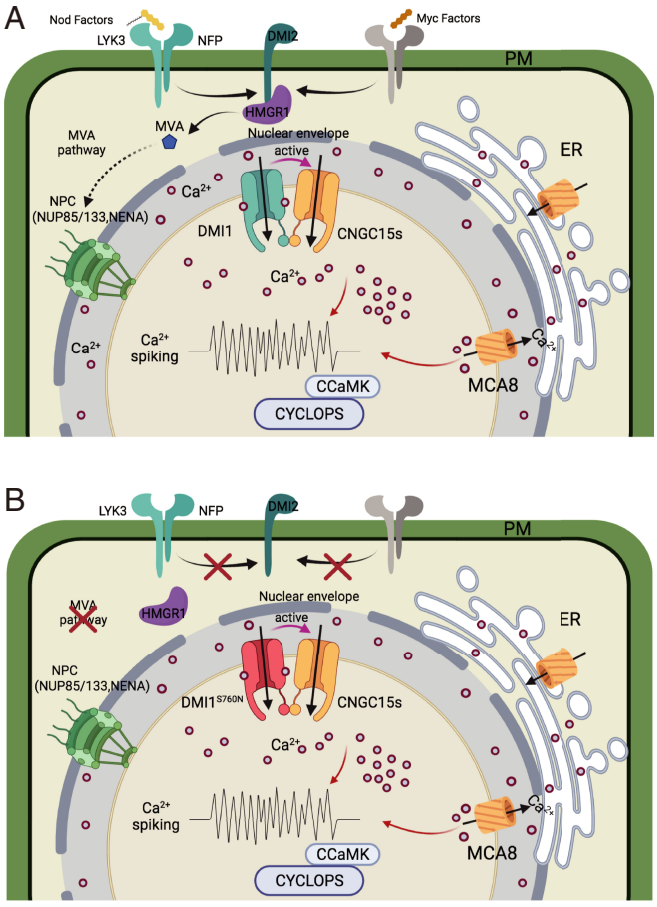

Fig. 7. Proposed model for DMI1 and CNGC15 in encoding Ca^{2+} oscillations during symbiotic interactions. NF or Myc factor is perceived by its plasma membrane receptors, leading to activation of a second messenger, which may be mevalonate. Subsequently, nuclear membrane–localized DMI1 is activated, which interacts with CNGC15s to enhance calcium influx, triggering nuclear calcium spiking, which is decoded by the CCaMK–CYCLOPS complex (*A*). In gain-of-function DMI1, constitutive interaction with CNGC15s and enhancement of CNGC15 channel activity lead to constitutive nuclear Ca^{2+} spiking (*B*). Images were created with BioRender (https://biorender.com).

Materials and Methods

Plant Material, Bacterial Strains, and Growth Conditions. *Medicago truncatula* cv. *Jemalong* A17 and R108 were used as WT, and mutants *nfp-1*, *dmi2-1*, *cngc15b-1* (NF10831), *cngc15c-1* (NF5069), *dmi3-1*, *ern1-1*, and *nin-1* were used in this study. *ENOD11*p:GUS and YC3.6 were incorporated into *spd1* through crossing with an existing, stable *M. truncatula ENOD11*p:GUS or YC3.6 line. *S. meliloti* 1021 (Sm1021) carrying *lacZ* (pXLGD4:*lacZ*) was used for inoculation. *Agrobacterium rhizogenes* strain AR1193 was used to transform *M. truncatula*, and *A. tumefaciens* strain EHA105 was used to express proteins in *Nicotiana benthamiana*. HEK293T cells were used for Ca^{2+} imaging. Yeast strain AH109 was used for yeast two-hybrid assays. Yeast strain *Pichia pastoris* GS115 was used for protein expression.

M. truncatula seeds were scarified for 8 to 10 min either in concentrated sulfuric acid or using sandpaper. After removing the sulfuric acid, the seeds were rinsed three times with sterilized water. Then, the seeds were surface-sterilized in 10% sodium hypochlorite for 2 min, washed five times in sterilized water, and left for 2 h in sterilized water to imbibe. Imbibed seeds were transferred to 1.5% water agar plates and kept at 4 °C for 2 d, and then grown at 22 °C for 1 to 2 d before germination. Seedlings were then grown on BNM or a 1:1 mixture of vermiculite and perlite. Plants were incubated in controlled-environment rooms at 22 °C and 80% humidity. *N. benthamiana* was grown in a growth chamber, and 3- to 4-wk-old plants were used for protein expression.

Mutant Screen and Double-Mutant Generation. *dmi2-1* was mutagenized by ethyl methanesulfonate and the M_2 seeds were used for suppressor screening. Approximately 500 M_2 family seeds (more than 50,000 individual plants) were inoculated with *Sm1021* and nodulation was screened 4 wk after inoculation. Six lines were shown to produce white nodules; however, all were later demonstrated to be *spd1*. For phenotyping, WT and *spd1* M2 seedlings were grown on BNM plates or sterile N-free mixtures (vermiculite and perlite).

To generate double mutants, homozygous *spd1* was crossed with *nfp-1*, *dmi3-1*, *ern1-1*, or *nin-1* mutants. The F_1 plants were self-crossed and the double mutants were scored in the F_2 generation using the primers indicated in *SI Appendix*, Table S3.

Gene Isolation. The mutant (*dmi2 spd1*) was backcrossed with *M. truncatula* A17, and resultant F_1 plants formed white nodules in the absence of rhizobia. The *spd1* single mutant was then isolated and used for further experiments. The candidate gene was isolated using a map-based cloning and deep-sequencing approach. *spd1* was crossed with *M. truncatula* A20, and the spontaneous nodulation phenotype was scored in F_2 progeny from self-pollinated F_1 plants. *spd1* is a dominant mutation, and therefore Nod^- plants were used for rough mapping. Genomic DNA was extracted and simple sequence repeat markers were used for rough mapping. Then, next-generation sequencing was used on bulked segregants to fine-map the candidate gene. Two DNA bulks for sequencing were made from the F_2 mapping population. Bulks W (WT) and M (mut) were made by mixing equal amounts of DNA from 40 Nod^- and 149 Nod^+ plants, respectively. The libraries were constructed using the TruSeq Nano DNA LT Sample Preparation Kit (Illumina), and then sequenced on the Illumina HiSeq X Ten platform (Illumina). Clean reads were aligned to the reference genome (*M. truncatula* v3.5) using the Burrows–Wheeler aligner (version 0.7.12) with default options. The sequence analysis was performed by Oebiotech.

RNA-Seq and Data Analysis. $spd1^{+/-}$ seedlings were grown in BNM and roots with tiny bumps were harvested at 7 d after germination. WT (A17) seedlings were grown in BNM in a square plate and inoculated with *Sm1021* after 2 d, and then roots were harvested 5 dpi. RNA-seq was performed by Novogene. The libraries for RNA-seq were prepared by the Library Prep Kit (NEBNext Ultra RNA), and were sequenced using Illumina. Reads from the RNA-seq experiments provided as raw fastq data were quality-controlled and mapped to *M. truncatula* reference genome version 4.0 (Mt4.0v1). At least three biological replicates were always included in the full analysis. DEGs were identified by pairwise comparisons of expression levels (total exon reads) using NovoMagic v3.0 (https://magic.novogene.com/customer/main), a data analysis cloud platform independently

developed by Novo Zhiyuan. For further analyses, only DEGs with a $\log_2$ fold change larger than 1 and a false discovery rate–corrected *P* value smaller than 0.05 were considered. RNA-seq data were compared for *spd1*$^{+/-}$, WT 5 dpi, WT 4 h, NF 4 and 20 h (39), and AMF (30).

Gene Expression Analysis. For gene expression, germinated *spd1* seedlings were grown on BNM plates, and then heterozygous *spd1* (*spd1*$^{+/-}$) was harvested at 1, 7, or 21 d after germination. To harvest *spd1* at 1 d after germination, the individual plants were genotyped using the primers in *SI Appendix*, Table S3 before harvesting. To harvest material at 7 d or 3 wk after germination, heterozygous *spd1* was identified as having long roots and spontaneous nodules, while homozygous *spd1* was identified as having short roots and few spontaneous nodules.

RNA extraction and qRT-PCR were performed as described previously (40).

spd1 was crossed with an *ENOD11*p:GUS stable line, and the F_1 plants had GUS and bumps and were grown to produce seeds. F_2 plants with a heterozygous or homozygous *spd1* were used for GUS staining.

Calcium Spiking. *spd1* was crossed with YC3.6 stable lines, and the F_2 plants were scored. The *CNGC15b* RNAi vector, which utilized the pK7GW1WG2D (II) backbone containing a DsRED selection marker, was expressed in *spd1*$^{+/-}$ YC3.6 through hairy root transformation. Heterozygous or homozygous *spd1* carrying YC3.6 root cells were imaged on a TE2000-U inverted microscope (Nikon) equipped with a Spectra-X Light Engine (Lumencor). Cameleon was excited at a wavelength of 458 nm and captured with an electron-multiplying charge-coupled device camera (model ImagEM-1K camera, Hamamatsu). Emitted fluorescence was separated using an image splitter with a dichroic mirror (model Optosplit II, Cairn Research) and then passed through a cameleon filter set. Images were collected every 5 s with 1-s exposure and analyzed using MetaFluor software (Molecular Devices). The time-lapse images were saved as TIF graphic files and the pseudocolor ratio images were processed using ImageJ software (41).

Root Hair Deformation and Rhizobial Infection. For root hair deformation assays, germinated WT (A17) and *spd1*$^{+/-}$ seedlings were grown on BNM plates for 3 d, and then incubated with NF from *S. meliloti* 2011 or the rhizobia themselves for 24 to 36 h before analysis. Images were taken using a Nikon Eclipse Ni light microscope with a Nikon DS-Fi2 camera.

For rhizobial infection analysis, *M. truncatula* seedlings were transferred into a vermiculite and perlite mixture (1:1) and inoculated with *S. meliloti* 1021 carrying *HemA:LacZ* 5 to 7 d after germination. The infection and nodulation phenotypes were analyzed at the indicated time points by light microscopy (Eclipse Ni, Nikon) after histochemical root staining using X-gal.

Localization of DMI1^{S760N} in *M. truncatula*. DMI1 and DMI1^{S760N} in the binary vector pUb-3HA-GFP were transformed into *M. truncatula* WT roots using hairy root transformation. GFP fluorescence was used to identify transgenic roots with a fluorescence stereomicroscope (SMZ1500, Nikon) 3 wk after transformation; plants with transgenic roots were transferred to square Petri dishes (100 × 100 mm) on MFP medium. The roots were collected and previously described methods were followed for immunofluorescence localization (42, 43). Hemagglutinin (Huiou Biotech, HOA012HA01) was used as primary antibody, and Cy3 AffiniPure goat anti-mouse immunoglobulin G (H+L) (Jackson ImmunoResearch, CAS115-165-003) was used as the immunofluorescence secondary antibody. The fluorescence images were captured with a confocal microscope (TCS SP8, Leica), and the nucleus was stained by DAPI.

Protein Expression and Purification. DNA encoding the soluble domain (residues 343 to 882) of *M. truncatula* DMI1 (UniProt ID code Q6RHR6) was subcloned into the pPICZ-C vector with a TEV protease cleavage site and a GFP-His_6 tag at the C-terminal end. The vector was linearized with *Pme*I restriction enzyme and incorporated into *P. pastoris* strain GS115 by electroporation. Positive clones were selected on agar plates containing 100 μg/mL zeocin (Invitrogen). Transformed cells were grown in MGYH medium to an OD_{600} of 5.0 and then to induction medium MMH for 48 h at 27 °C to induce protein expression. Cells were harvested and resuspended in buffer A (20 mM Tris, pH 8.0, 100 mM NaCl, 5% glycerol) supplemented with 1 mM phenylmethylsulfonyl fluoride (PMSF), 2 mM Mg^{2+}, and 5 μg·mL^{-1} DNase, and homogenized with UH-06 (Union-Biotech) six times at 17,000 psi. The cell lysate was centrifuged at 20,000 × *g* for 1 h, and the supernatant was loaded onto an Ni-NTA column and washed with buffer A supplemented with 20 mM imidazole. The protein was eluted from the column using buffer A supplemented with 250 mM imidazole and TEV protease was added to remove GFP at 4 °C for 48 h. Proteins were concentrated using an Amicon Ultra 50K filter (Merck Millipore) and further purified by Superdex 200 Increase 10/30 GL (GE Healthcare) in buffer B (20 mM Tris, pH 8.0, 100 mM NaCl). The peak fraction was concentrated to 5 to 6 mg·mL^{-1} for crystallization.

Crystallization, Data Collection, and Determination of Structure. Crystals were grown at 4 °C for about 1 wk using the sitting drop vapor diffusion method, by mixing with reservoir solution (16% [weight/volume (vol)] polyethylene glycol (PEG) 4000, 0.2 M KCl, 0.01 M $CaCl_2$, 0.05 M sodium cacodylate trihydrate, pH 5.4) at a 1:1 ratio. The crystals were cryoprotected by serial transfers into reservoir solutions supplemented with 30% (vol/vol) glycerol, and flash-cooled in liquid nitrogen. Data collection was performed at the BL19U1 beamline of the Shanghai Synchrotron Radiation Facility. The data were processed with HKL-3000 (44), and the initial phase was determined by molecular replacement with Phenix (45), using the crystal structure of the LjCASTOR gating ring (Protein Data Bank ID code 6O6J) as a template. The MtDMI1 RCK domain was built in Coot (46), and then refined by iterative rounds of manual adjustment with Coot and refinement with Phenix. Data collection and structure refinement statistics are shown in *SI Appendix*, Table S2.

Calcium Imaging Assay in HEK293T Cells. The HEK293T cell calcium imaging assay was done as described previously with small modifications (47). Briefly, the coding sequences of DMI1, DMI1^{S760N}, CNGC15b, and CNGC15c were fused to the YC3.6 C terminus and then inserted into the vector pCI-neo. DMI^{R448A}, DMI1$^{S760N\ E521A}$, DMI1$^{S760N\ D293N}$, CNGC15b^{R504Q}, or CNGC15b^{G346E} were generated with a site-mutagenesis kit. The corresponding combinations were cotransfected into HEK293T cells, and bright YC3.6 fluorescence was captured and the ratio 535 nm/480 nm was monitored using an Olympus inverted microscope (IX71) with a 40× objective. Prior to Ca^{2+} imaging, transfected HEK293T cells were cultured in a CO_2 incubator at 37 °C for 2 d. After adjusting the focal length, the typical cells with good YC3.6 fluorescence were selected by MAG Biosystems 7.5 (MetaMorph) for data acquisition and analysis. The wavelengths used to monitor the fluorescence resonance energy transfer (FRET)/cyan fluorescent protein (CFP) light ratio were 535 nm/442 nm, the interval of data acquisition was 4 s, and exposure time was 30 ms. The standard external working solution for Ca^{2+} imaging contained 120 mM NaCl, 10 mM glucose, 10 mM Hepes, 3 mM KCl, 1.2 mM $NaHCO_3$, and 1 mM $MgCl_2$; the pH was adjusted to 7.2 with NaOH, and external Ca^{2+} was added as indicated. All primer sequences for vector construction are listed in *SI Appendix*, Table S3. The number of cells detected by real-time fluorescence was more than 30.

Additional materials and methods including hairy root transformation in *M. truncatula*, qRT-PCR analysis, and protein interaction assays are described in *SI Appendix, Materials and Methods*.

Data, Materials, and Software Availability. Raw and processed RNA-seq data reported in this article have been deposited in the Genome Sequence Archive database in the National Genomics Data Center, https://ngdc.cncb.ac.cn/ (accession no. CRA005185) (48). The atomic coordinates and structure factors for DMI1 reported in this article have been deposited in the Protein Data Bank (ID code 7VM8) (49).

All plant materials are available upon request.

All study data are included in the article and/or *SI Appendix*.

ACKNOWLEDGMENTS. We thank Prof. Allan J. Downie (John Innes Centre, UK) and Jeremy D. Murray (Center for Excellence in Molecular Plant Sciences, Chinese Academy of Sciences [CAS], China) for manuscript editing and useful discussions, Prof. Jiming Gong (Center for Excellence in Molecular Plant Sciences, CAS, China) and Shujia Zhu (Center for Excellence in Brain Science and Intelligence Technology, CAS, China) for helping with Ca^{2+} imaging, and Prof. Jianghua Chen (Xishuangbanna Tropical Botanical Garden, CAS, China) for helping with map-based cloning. This work was supported by the CAS Project for Young Scientists in Basic Research (YSBR-011), National Key R&D Program of China (2016YFA0500500), National Natural Science Foundation of China (32170243), Strategic Priority Research Program of the CAS (XDB27040208), Bill and Melinda Gates Foundation, and the Foreign, Commonwealth and Development Office as OPP1028264, Engineering Nitrogen Symbiosis for Africa.

Author affiliations: [a]National Key Laboratory of Plant Molecular Genetics,Chinese Academy of Sciences Center for Excellence in Molecular Plant Sciences, Shanghai Institute of Plant Physiology and Ecology, Chinese Academy of Sciences, Shanghai, 200032, China; [b]University of the Chinese Academy of Sciences, Beijing, 100049, China; and [c]Sainsbury Laboratory, University of Cambridge, 47 Bateman Street, Cambridge, CB2 1LR, United Kingdom

1. G. Truchet *et al.*, Sulphated lipo-oligosaccharide signals of *Rhizobium meliloti* elicit root nodule organogenesis in alfalfa. *Nature* **351**, 670–673 (1991).
2. M. K. Ried, M. Antolín-Llovera, M. Parniske, Spontaneous symbiotic reprogramming of plant roots triggered by receptor-like kinases. *eLife* **3**, e03891 (2014).
3. S. Saha, A. Dutta, A. Bhattacharya, M. DasGupta, Intracellular catalytic domain of symbiosis receptor kinase hyperactivates spontaneous nodulation in absence of rhizobia. *Plant Physiol.* **166**, 1699–1708 (2014).
4. L. Tirichine *et al.*, Deregulation of a Ca^{2+}/calmodulin-dependent kinase leads to spontaneous nodule development. *Nature* **441**, 1153–1156 (2006).
5. C. Gleason *et al.*, Nodulation independent of rhizobia induced by a calcium-activated kinase lacking autoinhibition. *Nature* **441**, 1149–1152 (2006).
6. S. Singh, K. Katzer, J. Lambert, M. Cerri, M. Parniske, CYCLOPS, a DNA-binding transcriptional activator, orchestrates symbiotic root nodule development. *Cell Host Microbe* **15**, 139–152 (2014).
7. T. Soyano, H. Kouchi, A. Hirota, M. Hayashi, Nodule inception directly targets NF-Y subunit genes to regulate essential processes of root nodule development in *Lotus japonicus*. *PLoS Genet.* **9**, e1003352 (2013).
8. T. Vernié *et al.*, The NIN transcription factor coordinates diverse nodulation programs in different tissues of the *Medicago truncatula* root. *Plant Cell* **27**, 3410–3424 (2015).
9. K. Markmann, M. Parniske, Evolution of root endosymbiosis with bacteria: How novel are nodules? *Trends Plant Sci.* **14**, 77–86 (2009).
10. D. W. Ehrhardt, R. Wais, S. R. Long, Calcium spiking in plant root hairs responding to *Rhizobium* nodulation signals. *Cell* **85**, 673–681 (1996).
11. M. Chabaud *et al.*, Arbuscular mycorrhizal hyphopodia and germinated spore exudates trigger Ca^{2+} spiking in the legume and nonlegume root epidermis. *New Phytol.* **189**, 347–355 (2011).
12. R. J. Wais *et al.*, Genetic analysis of calcium spiking responses in nodulation mutants of *Medicago truncatula*. *Proc. Natl. Acad. Sci. U.S.A.* **97**, 13407–13412 (2000).
13. G. E. Oldroyd, Speak, friend, and enter: Signalling systems that promote beneficial symbiotic associations in plants. *Nat. Rev. Microbiol.* **11**, 252–263 (2013).
14. S. A. Walker, V. Viprey, J. A. Downie, Dissection of nodulation signaling using pea mutants defective for calcium spiking induced by Nod factors and chitin oligomers. *Proc. Natl. Acad. Sci. U.S.A.* **97**, 13413–13418 (2000).
15. M. Charpentier *et al.*, *Lotus japonicus* CASTOR and POLLUX are ion channels essential for perinuclear calcium spiking in legume root endosymbiosis. *Plant Cell* **20**, 3467–3479 (2008).
16. J. M. Ané *et al.*, *Medicago truncatula* DMI1 required for bacterial and fungal symbioses in legumes. *Science* **303**, 1364–1367 (2004).
17. S. Kim *et al.*, Ca^{2+}-regulated Ca^{2+} channels with an RCK gating ring control plant symbiotic associations. *Nat. Commun.* **10**, 3703 (2019).
18. M. Charpentier *et al.*, Nuclear-localized cyclic nucleotide-gated channels mediate symbiotic calcium oscillations. *Science* **352**, 1102–1105 (2016).
19. W. Capoen *et al.*, Nuclear membranes control symbiotic calcium signaling of legumes. *Proc. Natl. Acad. Sci. U.S.A.* **108**, 14348–14353 (2011).
20. A. Edwards, A. B. Heckmann, F. Yousafzai, G. Duc, J. A. Downie, Structural implications of mutations in the pea SYM8 symbiosis gene, the DMI1 ortholog, encoding a predicted ion channel. *Mol. Plant Microbe Interact.* **20**, 1183–1191 (2007).
21. M. Matzke, T. M. Weiger, I. Papp, A. J. Matzke, Nuclear membrane ion channels mediate root nodule development. *Trends Plant Sci.* **14**, 295–298 (2009).
22. M. Venkateshwaran *et al.*, The recent evolution of a symbiotic ion channel in the legume family altered ion conductance and improved functionality in calcium signaling. *Plant Cell* **24**, 2528–2545 (2012).
23. Z. Kevei *et al.*, 3-hydroxy-3-methylglutaryl coenzyme A reductase 1 interacts with NORK and is crucial for nodulation in *Medicago truncatula*. *Plant Cell* **19**, 3974–3989 (2007).
24. M. Venkateshwaran *et al.*, A role for the mevalonate pathway in early plant symbiotic signaling. *Proc. Natl. Acad. Sci. U.S.A.* **112**, 9781–9786 (2015).
25. B. J. Sieberer, M. Chabaud, J. Fournier, A. C. Timmers, D. G. Barker, A switch in Ca^{2+} spiking signature is concomitant with endosymbiotic microbe entry into cortical root cells of *Medicago truncatula*. *Plant J.* **69**, 822–830 (2012).
26. E. M. Engstrom, D. W. Ehrhardt, R. M. Mitra, S. R. Long, Pharmacological analysis of Nod factor-induced calcium spiking in *Medicago truncatula*. Evidence for the requirement of type IIA calcium pumps and phosphoinositide signaling. *Plant Physiol.* **128**, 1390–1401 (2002).
27. W. Capoen *et al.*, Calcium spiking patterns and the role of the calcium/calmodulin-dependent kinase CCaMK in lateral root base nodulation of *Sesbania rostrata*. *Plant Cell* **21**, 1526–1540 (2009).
28. I. Damiani *et al.*, Nod factor effects on root hair-specific transcriptome of *Medicago truncatula*: Focus on plasma membrane transport systems and reactive oxygen species networks. *Front. Plant Sci.* **7**, 794 (2016).
29. E. P. Journet *et al.*, *Medicago truncatula* ENOD11: A novel RPRP-encoding early nodulin gene expressed during mycorrhization in arbuscule-containing cells. *Mol. Plant Microbe Interact.* **14**, 737–748 (2001).
30. L. H. Luginbuehl *et al.*, Fatty acids in arbuscular mycorrhizal fungi are synthesized by the host plant. *Science* **356**, 1175–1178 (2017).
31. W. Tian *et al.*, A calmodulin-gated calcium channel links pathogen patterns to plant immunity. *Nature* **572**, 131–135 (2019).
32. Q. F. Gao *et al.*, Cyclic nucleotide-gated channel 18 is an essential Ca^{2+} channel in pollen tube tips for pollen tube guidance to ovules in *Arabidopsis*. *Proc. Natl. Acad. Sci. U.S.A.* **113**, 3096–3101 (2016).
33. L. Tirichine *et al.*, A gain-of-function mutation in a cytokinin receptor triggers spontaneous root nodule organogenesis. *Science* **315**, 104–107 (2007).
34. Y. Pan *et al.*, Dynamic interactions of plant CNGC subunits and calmodulins drive oscillatory Ca^{2+} channel activities. *Dev. Cell* **48**, 710–725.e5 (2019).
35. A. Zhang *et al.*, S-type anion channels SLAC1 and SLAH3 function as essential negative regulators of inward K^+ channels and stomatal opening in *Arabidopsis*. *Plant Cell* **28**, 949–955 (2016).
36. T. Soyano, H. Hirakawa, S. Sato, M. Hayashi, M. Kawaguchi, Nodule inception creates a long-distance negative feedback loop involved in homeostatic regulation of nodule organ production. *Proc. Natl. Acad. Sci. U.S.A.* **111**, 14607–14612 (2014).
37. M. Maekawa-Yoshikawa *et al.*, The temperature-sensitive brush mutant of the legume *Lotus japonicus* reveals a link between root development and nodule infection by rhizobia. *Plant Physiol.* **149**, 1785–1796 (2009).
38. D. M. Chiasson *et al.*, A quantitative hypermorphic *CNGC* allele confers ectopic calcium flux and impairs cellular development. *eLife* **6**, e25012 (2017).
39. K. Schiessl *et al.*, Nodule inception recruits the lateral root developmental program for symbiotic nodule organogenesis in *Medicago truncatula*. *Curr. Biol.* **29**, 3657–3668.e5 (2019).
40. Z. Luo *et al.*, NLP1 reciprocally regulates nitrate inhibition of nodulation through SUNN-CRA2 signaling in *Medicago truncatula*. *Plant Commun.* **2**, 100183 (2021).
41. M. D. Abramoff, P. J. Magalhães, S. J. Ram, Image processing with ImageJ. *Biophotonics Int.* **11**, 36–42 (2004).
42. M. Sauer, T. Paciorek, E. Benková, J. Friml, Immunocytochemical techniques for whole-mount in situ protein localization in plants. *Nat. Protoc.* **1**, 98–103 (2006).
43. M. Liu *et al.*, CERBERUS is critical for stabilization of VAPYRIN during rhizobial infection in *Lotus japonicus*. *New Phytol.* **229**, 1684–1700 (2021).
44. W. Minor, M. Cymborowski, Z. Otwinowski, M. Chruszcz, HKL-3000: The integration of data reduction and structure solution–From diffraction images to an initial model in minutes. *Acta Crystallogr. D Biol. Crystallogr.* **62**, 859–866 (2006).
45. P. D. Adams *et al.*, PHENIX: A comprehensive Python-based system for macromolecular structure solution. *Acta Crystallogr. D Biol. Crystallogr.* **66**, 213–221 (2010).
46. P. Emsley, K. Cowtan, Coot: Model-building tools for molecular graphics. *Acta. Crystallogr. D Biol. Crystallogr.* **60**, 2126–2132 (2004).
47. Q. F. Gao, C. F. Fei, J. Y. Dong, L. L. Gu, Y. F. Wang, *Arabidopsis* CNGC18 is a Ca^{2+}-permeable channel. *Mol. Plant* **7**, 739–743 (2014).
48. H. Liu *et al.*, CRA005185, data for "Constitutive activation of a nuclear-localized calcium channel complex in *Medicago truncatula*." National Genomics Data Center. https://ngdc.cncb.ac.cn/search/?dbId=gsa&q=CRA005185&page=1. Accessed 5 August 2022.
49. H. Liu *et al.*, 7VM8, data for "Constitutive activation of a nuclear-localized calcium channel complex in *Medicago truncatula*." PDB. https://www.rcsb.org/structure/unreleased/7VM8. Deposited 8 October 2021.